2022

Modelling and operational management of the Dawson Pit 6-8 lowwall instability

Matt Tsang
Anglo American Metallurgical Coal

Leonie Bradfield
Bradfield Mining Geotechnics

Jafnie Muhsin
Anglo American Metallurgical Coal

Ian Colbourne
Anglo American Metallurgical Coal

Shuaibu Bun-Seisay
Anglo American Metallurgical Coal

See next page for additional authors

MODELLING AND OPERATIONAL MANAGEMENT OF THE DAWSON PIT 6-8 LOWWALL INSTABILITY

Matthew Tsang[1], Leonie Bradfield[2], Jafnie Muhsin[3], Ian Colbourne[4], Shuaibu Bun-Seisay[5], Hannah Kelly[6] and Gift Makusha[7]

ABSTRACT: A case study of a deep-seated spoil lowwall instability controlled by a classical active-passive wedge mechanism at Anglo American Metallurgical Coal's Dawson Mine is presented. Following a truck dump extension, widespread displacements were identified during conventional single forward pass de-coaling of Pit 6-8 strip E15. New through-spoil drilling, downhole geophysical logging, and XRD analysis identified a moisture-sensitive tuffaceous claystone unit containing a high proportion of medium-high swelling, mixed-layer illite-smectite clays 11-12 m below the lowwall floor. A novel soil mechanics approach was used to determine the mechanical properties of the tuffaceous claystone for which conventional rock mechanics tests could not be applied. Three-dimensional numerical modelling was then undertaken in FLAC3D to: a) validate the characterised mechanical properties; b) determine appropriate buttress slot widths for retreat mining of strip E16; and c) provide a validated base case for the predictive modelling and design of future strips. Operational controls for mining of strip E16 included: surface monitoring (radar, LiDAR); subsurface monitoring (TDR, VWPs); and an adaptive mine plan following the Observational Method. The TDR confirmed that the tuffaceous claystone unit at 11-12 m depth was acting as the sole basal horizon controlling the instability and mining of strip E16 was completed safely without coal sterilisation.

INTRODUCTION

Slope instability has potentially serious consequences if uncontrolled. In open cut coal mining, spoil lowwall instabilities are often active-passive wedge mechanisms in which the self-weight of an up-dip active spoil wedge drives a down-dip passive wedge along a weak basal unit below the coal seam floor (**Figure 1**). Due to the typically high degree of continuity of the weak basal floor units, the extents of such instabilities can be large and involving potentially millions of cubic metres of spoil. This is often further exacerbated by the encroachment of advancing truck dumps beyond the limits of stability, which are generally unknown until they begin to manifest as tension cracks in the slope. At this point, strains/displacements are plastic and irrecoverable and it is therefore too late to modify the slope design to eliminate the instability. Further operation in the vicinity of the unstable slope is then contingent on engineering and administrative controls which are less effective and inevitably reduce production rates. While modern technologies such as slope stability radars and unmanned aerial vehicles have greatly reduced safety incidents related to spoil lowwall instability, the economic consequences have remained largely unchanged. Proactive identification of potential instability mechanisms via geotechnical investigation, rock mass characterisation, and slope stability analysis at the design stage is therefore the only effective way to mitigate the economic consequences of spoil lowwall instabilities. This paper presents a recent example of a large spoil lowwall instability at Anglo American Metallurgical Coal's (AAMC) Dawson Mine in which three-dimensional numerical modelling and operational controls were successfully employed to enable safe mining without coal sterilisation.

[1] *Geotechnical Specialist: Modelling, Anglo American Metallurgical Coal. Email:* matt.tsang@angloamerican.com
[2] *Director/Principal, Bradfield Mining Geotechnics. Email:* leonie@bradfieldgeotech.com.au
[3] *Geotechnical Specialist: Open Cut, Anglo American Metallurgical Coal. Email:* jafnie.muhsin@angloamerican.com
[4] *Geotechnical Engineer, Anglo American Metallurgical Coal. Email:* ian.colbourne@angloamerican.com
[5] *Geotechnical Engineer, Anglo American Metallurgical Coal. Email:* shuaibu.bunseisay@angloamerican.com
[6] *Graduate Geotechnical Engineer, Anglo American Metallurgical Coal. Email:* hannah.kelly@angloamerican.com
[7] *Manager Geotechnical, Anglo American Metallurgical Coal. Email:* gift.makusha@angloamerican.com

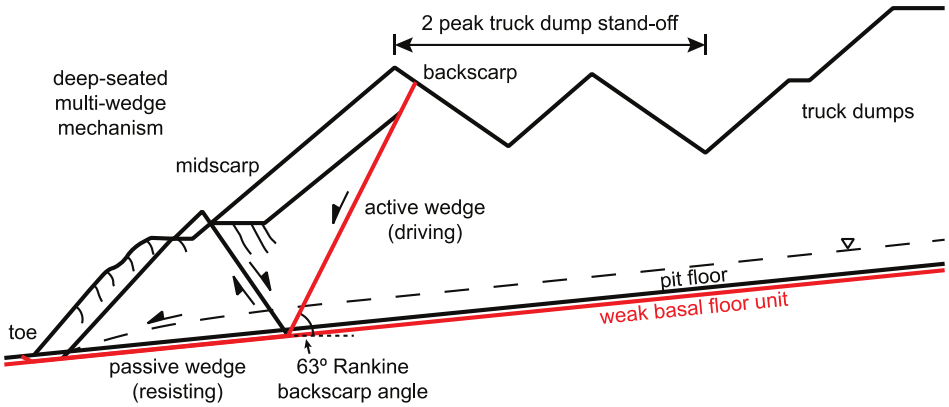

Figure 1: General lowwall active-passive wedge failure mechanism (modified from Simmons and McManus, 2004)

GEOLOGY

Stratigraphy

Dawson Mine is located in the Bowen Basin, approximately 200 km south-west of Gladstone, Queensland, on the eastern limb of the Mimosa Syncline. The project targets five coal seams (A, B, C, D, E in order of geological age from youngest to oldest) belonging to the late Permian-aged Baralaba Coal Measures (BCM, **Figure 2**). The seams dip broadly to the west at around 10° with several splits and coalescences. Interburden lithologies are predominantly alluvial floodplain facies consisting of litho-felspathic sandstone, siltstone, coal, and tuff (Leisemann et al., 1992). Underlying the BCM is the Kaloola Member (KM), which is characterised by abundant tuffs and thin, tuffaceous, non-economic coals interbedded with deltaic and prodeltaic siltstones and sandstones. The Kaloola Tuff, which is a stratigraphic marker horizon equivalent to the Yarrabee Tuff elsewhere in the Bowen Basin, is typically located within the E seam floor at a variable depth (Gonano, 1980).

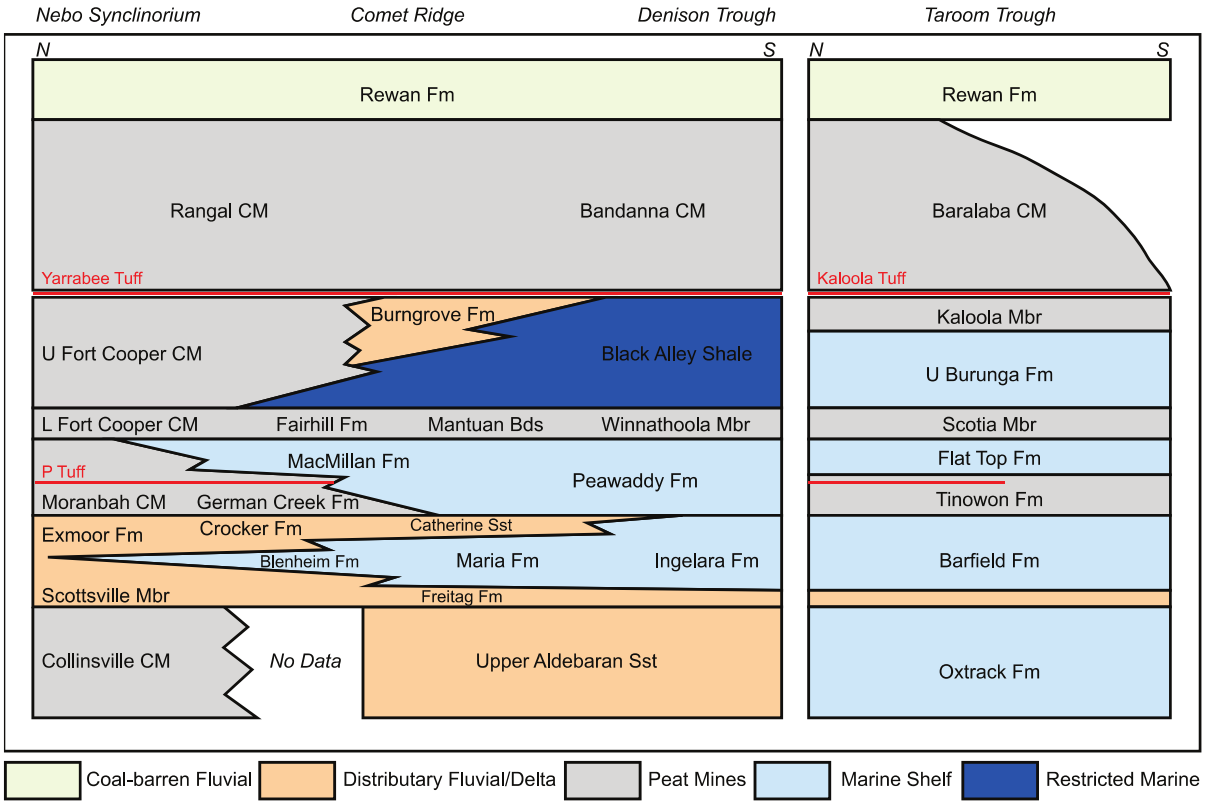

Figure 2: Stratigraphic supersequences and lithostratigraphic units in the Bowen Basin (modified from Sliwa and Esterle, 2015)

Structure

The main regional structures in the Dawson Mine area are NNW-trending, thin-skinned, low-angle thrusts representing the southern part of the Jellinbah Thrust Belt, albeit with diminished complexity and severity (Sliwa et al., 2008). A subordinate minor thrust system varying in strike from WNW to EW is also present and is possibly the result of reactivation of basement fault systems during compressional tectonism. Minor EW normal faults are also observed but tend to lack lateral continuity. Large cross-bedding structures are frequently encountered due to channel deposition and lateral migration discordant to seam structure. Other structures typical of a compressive tectonic environment and present in the Dawson Mine area include bedding plane shears, low-angle reverse faults, and thrust ramps with minor seam displacement. Locally within the pit 6-8 area, faults are NW-to-NNW trending thrusts.

STRIP E15 SLOPE PERFORMANCE

Following a truck dump extension, baseline linear creep of up to 2 mm/day was first detected in June 2018 in the strip E14 lowwall batter and spoil peaks from a routine comparison of monthly LiDAR survey scans (**Figure 3**). The truck dump extension consisted of a significant volume of waste material from double-strip mining of strips C15 and C16 and occurred prior to mining of strip E15 (**Figure 4**). Although tension cracks were not evident during initial inspections, over time they developed up to 800 m behind the lowwall toe and 1 km along strike, from the midpoint of the pit to the northern endwall. The pit then remained inactive with a buttress in place in the strip E14 void for the next 18 months, with mining of strip E15 commencing in February 2020 as a conventional single forward pass without backfilling. As de-coaling progressed and a greater strike length of slope was exposed, the rate of creep measured by radar monitoring gradually increased to an average of 2 mm/hr. Throughout mining of strip E15, multiple minor stress relief events of approximately 50 to 100 m strike length and 20 to 25 m height were observed in the lowwall batter with associated floor heave up to 5 m from the slope toe. Following floor disruption blasting of the E15 void, the lowwall displacement rate increased to a peak of 4 mm/hr but within 24 hours had regressed to the pre-blast rate of 2 mm/hr. The E15 void was then backfilled to preserve integrity of the lowwall while further analysis was undertaken for mining of E16.

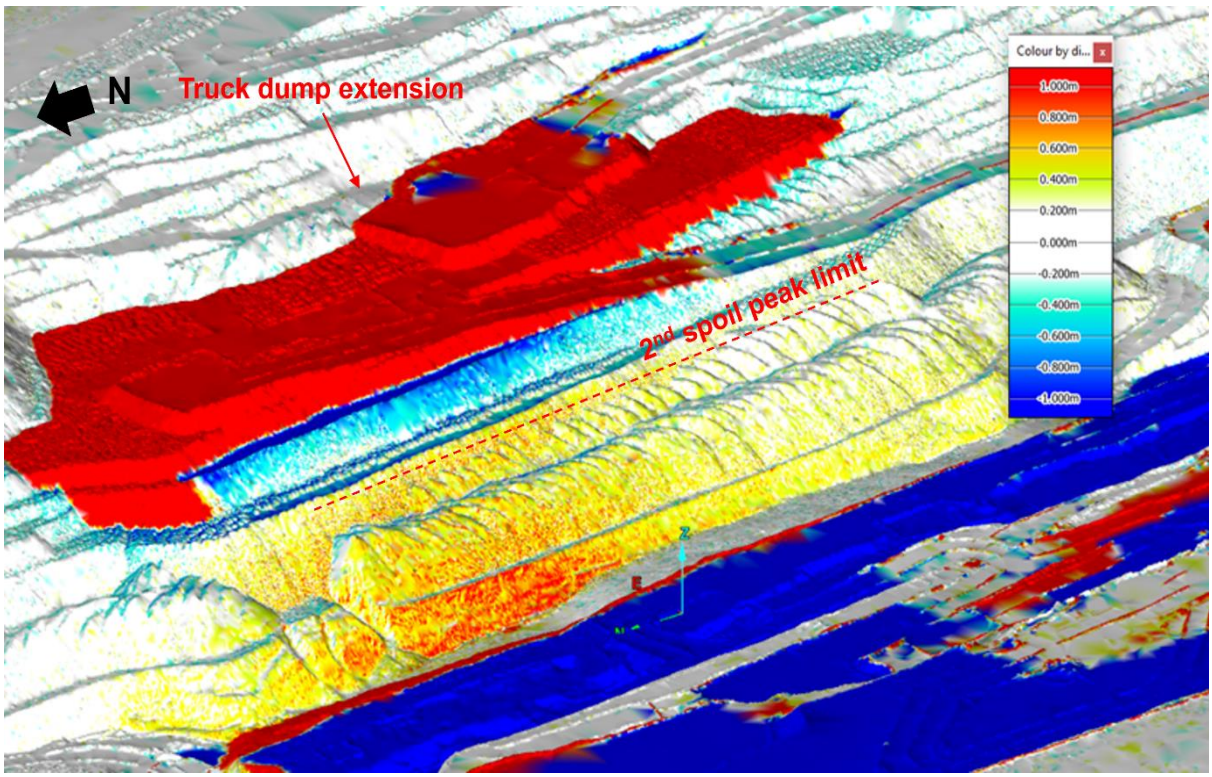

Figure 3: Proximity of strip C15-C16 truck dump extension to the 2nd dragline spoil peak limit and lowwall displacement magnitudes in the strip E14 lowwall

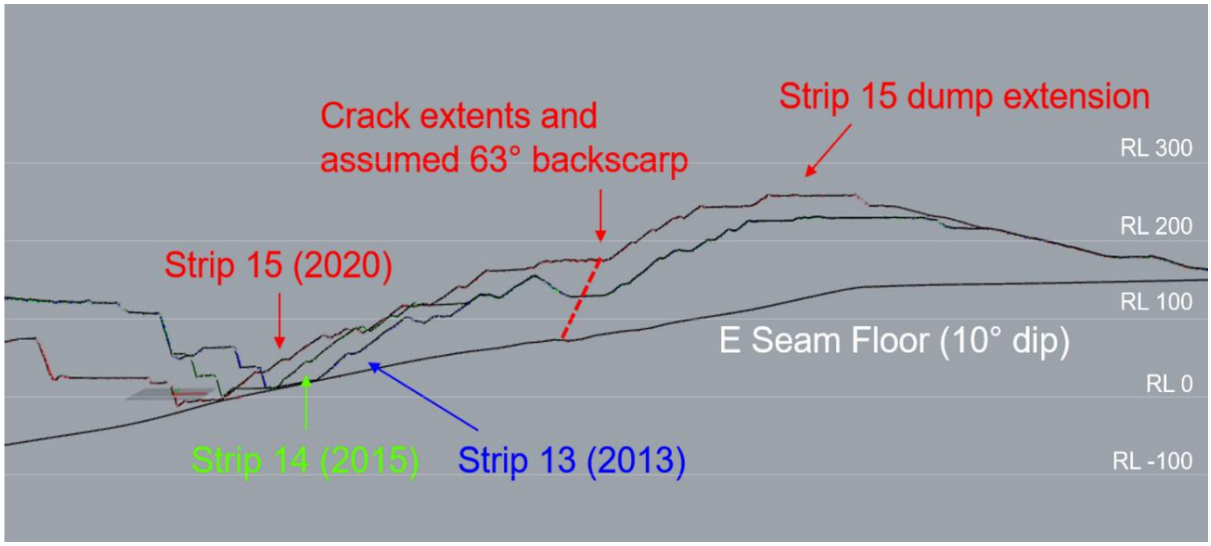

Figure 4: Configuration of Pit 6-8 strip 13-15 lowwall showing significant volume of additional spoil emplacement in strip 15 truck dump extension

ROCK MASS CHARACTERISATION

Additional Drilling

Interrogation of the Dawson exploration database revealed that geotechnical drilling data within the old Pit 6-8 lowwall footprint were sparse, with no geotechnical boreholes directly intercepting the region of instability found. This lack of data is believed to be related to several changes in mine ownership since it was established as Moura Mine in the 1960s and a recent lack of activity in Pit 6-8 while operations focused on the northern Terrace Pit. Slope stability analyses for strips E13 to E15 had assumed that any potential global slope instability mechanism would be controlled by a basal unit within the first 2 m of the E seam floor which had previously been logged as tuffaceous. However, these analyses had typically predicted Factors of Safety (FOS) in the range of 1.2 to 1.9 for various lowwall and truck dump configurations. This assumption was therefore brought into question following the instability in strip E15. Recognising that an unknown weak horizon in the E seam floor was potentially a contributing factor to the lowwall instability, site management approved the drilling of two new cored geotechnical boreholes to at least 20 m below the E seam floor:

- One through the spoil within the extents of the instability; and
- One in-pit, downdip of the lowwall toe.

Both boreholes were geophysically logged with the standard suite of tools, including: natural gamma, density, sonic velocity, and acoustic scanner. Competent rock core samples were sent for standard laboratory testing, including: Uniaxial Compressive Strength (UCS), Multi-stage Triaxial Compressive Strength (MTCS), Brazilian Tensile Strength (BTS), Direct Shear Strength (DSS), and Slake Durability (SD). Of particular interest was an approximately 300 mm thick, moisture-sensitive unit at a depth of 11.2 m below the E seam floor which had been logged as tuffaceous sandstone (**Figure 5**). The poor integrity of the specimen did not facilitate conventional rock mechanics tests and a novel soil mechanics approach was instead used to infer its shear strength properties. This involved X-Ray Diffraction (XRD) analysis to quantify the mineralogy coupled with Atterberg Limit (AL) tests to qualify the plasticity behaviour. In addition to the acquisition of geophysical logs and core samples for laboratory testing, both boreholes also served as instrumentation locations for monitoring of the rock mass and groundwater response to mining of strip E16. Arrays of Vibrating Wire Piezometers (VWPs) were installed in both boreholes to monitor groundwater pressures while a Time Domain Reflectometer (TDR) was installed in the spoil borehole to detect deep-seated shear displacements and confirm the horizon of the weak basal unit controlling the instability in response to mining.

Figure 5: Weak unit at a depth of 11.2 m below the E seam floor

Geophysics

A comparison of geophysical traces from the through-spoil borehole is shown in **Figure 6** with the following observations:

- A significant calliper deviation of up to 200 mm at the horizon coinciding with the weak unit observed in the drill core.
- A slight reduction in density and a slight increase in natural gamma at the weak unit horizon.
- The spoil borehole intersected the footprint of a previous floor disruption blast with the base of the blast influence zone coinciding with the top of the weak unit.
- The sonic velocity measurements appear to be erroneous at the weak unit horizon, possibly indicating blast-induced dilation.
- The rock mass below the weak unit is generally more competent, albeit with some isolated natural gamma spikes warranting further analysis.

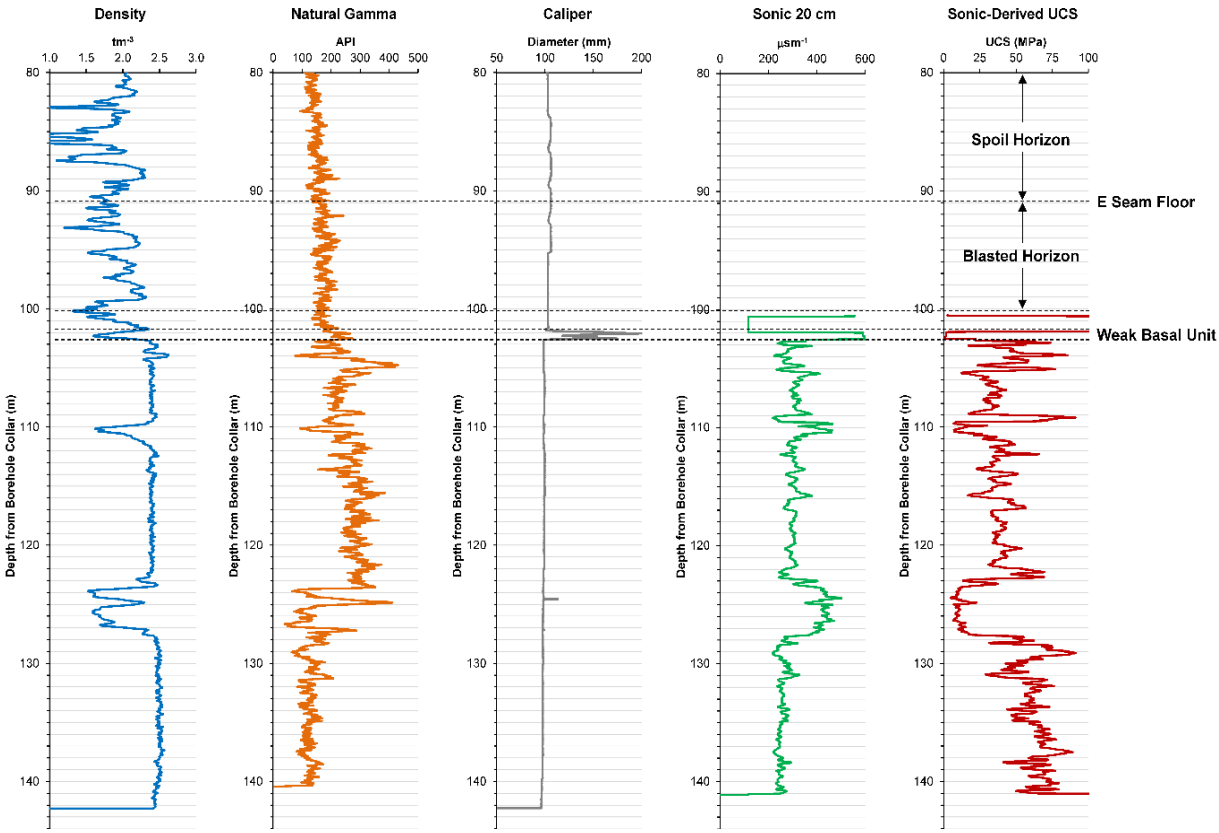

Figure 6: Comparison of geophysical traces from the spoil borehole within the extents of the instability showing a significant calliper deviation at the horizon of the weak unit

Laboratory Test Results

A comparison of UCS test results for the E seam floor and general Dawson overburden is presented in **Figure 7** by rock type and shows a strength reversal wherein sandstones are weaker than siltstones in the KM in the E seam floor but stronger above in the BCM. Reduced sandstone strengths are often related to a coarsening of the grain size but the E floor sandstones were all logged as very fine- to fine-grained. The problem was therefore inferred to be related to specific mineralogy and moisture sensitivity of KM sandstones that had not been previously encountered in the overlying BCM.

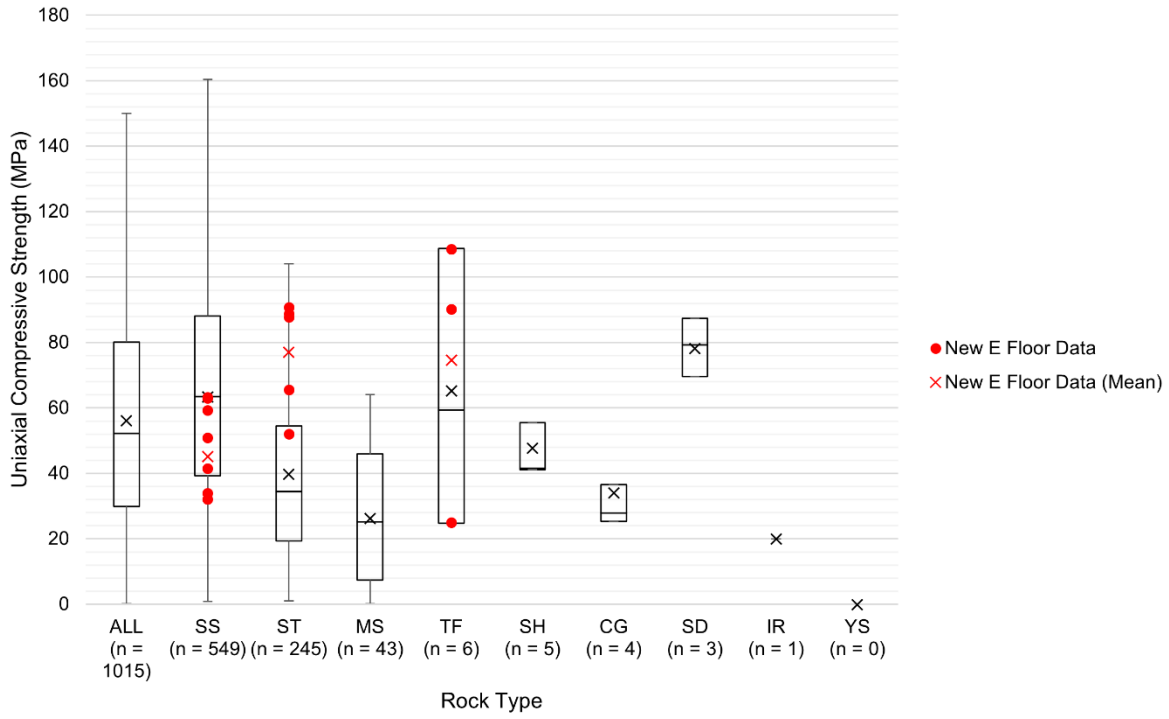

Figure 7: Comparison of the uniaxial compressive strength of the E seam floor and general Dawson overburden showing a reversal in the trend of sandstone and siltstone strengths

XRD and AL tests, which are not part of routine rock mass characterisation in the Australian coal mining industry, revealed:

- A unit within the first 2 m of the E seam floor that had historically been logged as a tuff was mineralogically a competent, quartzose sandstone and was unlikely to be the basal horizon controlling the large-scale instability as had been assumed in earlier design analyses.
- The moisture-sensitive weak unit at 11.2 m depth was comprised of a high proportion of tuffaceous, mixed layer illite-smectite swelling clays exhibiting high plasticity, and the lithology was therefore tuffaceous claystone, not tuffaceous sandstone as had originally been logged.

A summary of the E floor mineralogical composition determined by XRD analysis is provided in **Table 1**. A Casagrande chart developed from the AL test results is presented in **Figure 8** and shows that the tuffaceous claystone at 11.2 m depth was the most plastic sample of those tested. Similarly high plasticity horizons were also observed at depths of 5.5 m, 7.6 m, 9.9 m, 12.7 m, and 21.8 to 21.9 m, though these horizons were not as thick and did not correspond to caliper deviations. SD testing confirmed the high moisture sensitivity of the tuffaceous claystone unit at 11.2 m depth with a first cycle durability index of 2.2% and a second cycle durability index of 0.1%. A summary of SD durability indices by depth and rock type is provided in **Table 2** and shows additional horizons of moderate-to-high moisture sensitivity siltstones at depths of 12.7 m and 21.8 m.

Table 1: Summary of mineralogical composition of E seam floor determined by X-Ray Diffraction analysis

Depth below E Seam Floor (m)	Logged Lithology	Quartz (% weight)	Chlorite (% weight)	Calcite (% weight)	Calcite, Magnesian (% weight)	Muscovite (% weight)	Plagioclase Feldspar (% weight)	Potassium Feldspar (% weight)	Illite (% weight)	Mixed Layer Illite-Smectite (% weight)	Kaolinite (% weight)	Amorphous (% weight)
0.20	Tuff	59.5		2.8			4.1	3.7		23.0	2.8	3.7
0.20	Tuff	36.2	6.2				2.2	9.9		45.0		0.2
0.25	Tuff	67.8		1.6					10.0	7.0	6.6	6.7
0.25	Tuff	59.4		4.6			9.5		13.9	10.0		3.2
0.25	Tuff	53.8		11.4			8.4		11.8	9.0		5.6
1.00	Tuff	50.3	2.5	2.3			10.7	11.3		15.0		8.2
1.00	Tuff	36.5					1.6	17.0		44.0		0.6
1.10	Tuff	41.0			2.0	7.0	17.0	13.0		20.0		
1.40	Tuff	44.0			5.0	7.0	5.0	20.0		20.0		
1.70	Tuff	40.0	3.0			14.0	3.0	14.0		26.0		
2.70	Tuff	45.0			6.0	2.0	30.0	8.0		9.0		
3.80	Tuff	9.0			trace	28.0	2.0	17.0		44.0		
5.50	Tuff	23.0	5.0			27.0	trace	4.0		41.0		
6.40	Carb. Siltstone	32.0	1.0				14.0	51.0		2.0		
7.60	Tuff	17.0				29.0	3.0	11.0		40.0		
8.30	Siltstone	57.0	2.0		2.0	4.0	2.0	2.0		31.0		
8.60	Sandstone	50.0	trace		trace	16.0	4.0	1.0		29.0		
9.90	Sandstone	11.0	6.0		trace	6.0	22.0			55.0		
11.20	Tuffaceous Sandstone	1.0	13.0			6.0	10.0	7.0		63.0		
12.30	Tuff	35.0	7.0			1.0	6.0	6.0		45.0		
12.70	Siltstone	8.0	10.0	1.0		3.0	14.0	4.0		60.0		
21.80	Siltstone	23.0	1.0	trace			7.0	58.0		11.0		
21.90	Tuff	23.0	3.0		trace	15.0	4.0	3.0		52.0		
22.60	Tuff	30.0	3.0		6.0	23.0		4.0		34.0		
23.20	Tuff	1.0	1.0		68.0	trace		3.0		4.0	23.0	
25.30	Carb. Siltstone	19.0				22.0	4.0	10.0		45.0		
26.00	Tuff	25.0	1.0			13.0	2.0	21.0		38.0		
28.20	Sandstone	31.0	2.0		2.0	1.0	22.0	21.0		21.0		

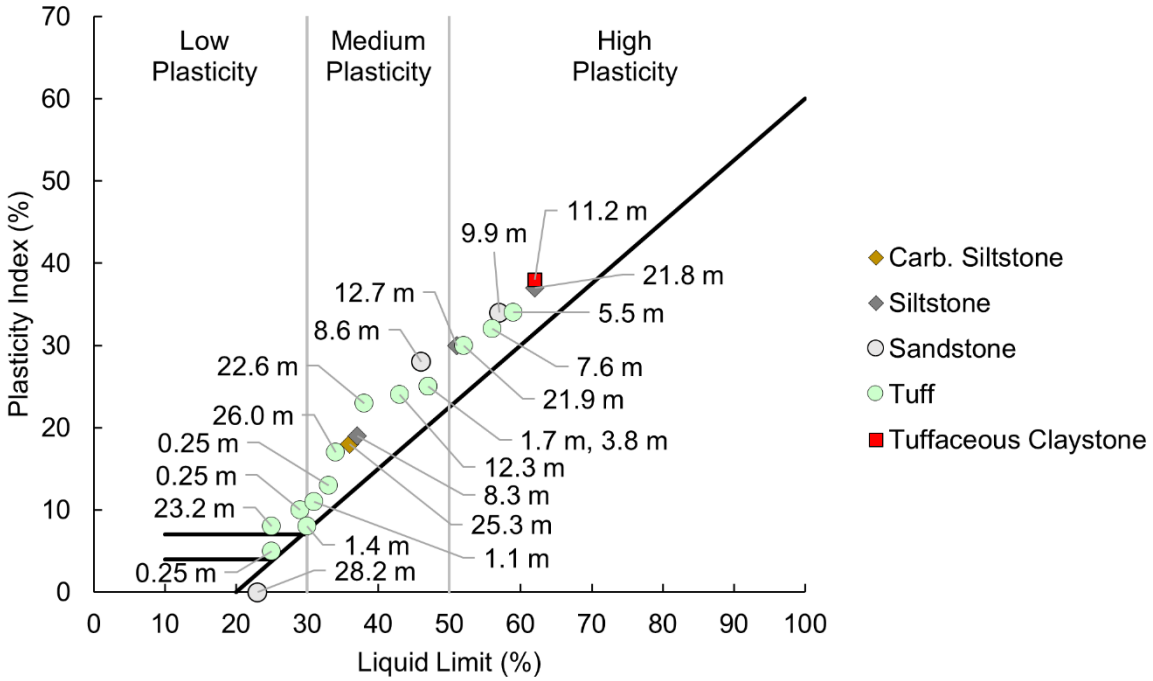

Figure 8: Casagrande plasticity chart by rock type with callout labels showing the depth of the sample below the E seam floor

Table 2: Summary of Slake Durability test results

Depth below E Seam Floor (m)	Logged Lithology	Durability Index, First Cycle (%)	Durability Index, Second Cycle (%)
1.1	Tuff	99.5	99.2
1.4	Tuff	99.1	98.8
8.3	Siltstone	98.3	97.4
8.6	Sandstone	97.7	96.4
11.2	Tuffaceous Sandstone*	2.2	0.1
12.7	Siltstone	46.0	26.1
21.8	Siltstone	31.2	17.7

*Revealed by XRD mineralogical analysis to be tuffaceous claystone.

Of the 13 total MTCS tests, only 3 returned valid Hoek-Brown constants, σ_{ci} and m_i, using the method of Hoek and Brown (1997). All laboratory test reports were subjected to internal quality control and the cause of the low success rate is not believed to be related to human or instrumentation error. Rather, it is believed to be an intrinsic limitation of the multi-stage method in which a single specimen is subjected to multiple load stages with the transition point between each stage manually identified by the technician from fluctuations in the load readout. These fluctuations relate to microfracture events representing new damage beyond the crack initiation stress (plasticity), and it is therefore inevitable that each successive stage will be loading the specimen with respect to a higher initial fracture intensity and thus lower achievable peak stress. Further, except for the final stage, the technician must stop each test stage prior to peak stress or else successive stages would be testing the specimen with respect to residual strength. The "peak" stresses measured in all stages prior to the final stage therefore lie somewhere between the crack initiation stress, which has been shown empirically to be 42-47% of peak stress (Brace et al., 1966; Nicksiar and Martin, 2013), and the achievable peak stress for the particular initial fracture intensity. This is a large stress range over which the technician may choose to transition the stage and the reliability of any Hoek-Brown constants derived from MTCS testing is therefore highly questionable.

As an alternative means of estimating m_i, the relationship with the compressive-tensile strength ratio, $\sigma_c/|\sigma_t|$, proposed by Hoek and Brown (2019) was used (Eq. 1). A correlation between compressive and tensile strengths measured from UCS and BTS tests respectively is presented in **Figure 9** and shows a

best-fit compressive-tensile strength ratio, $\sigma_c/|\sigma_t|$, of 8.6. This is slightly lower than the generic value of 10 that is often assumed. The equivalent uniaxial tensile strength, $|\sigma_t|$, in each case was obtained by multiplying the indirect Brazilian tensile strength by a factor of 0.7 after Perras and Diederichs (2014). An empirical m_i was then calculated locally for each $\sigma_c/|\sigma_t|$ and the results are summarised in **Table 3** alongside those measured from MTCS tests. In general, the empirically-derived m_i values tend to be lower than the measured values with averages of 9.7 and 11.9 respectively, though it is noted that the sample sizes were small (empirical n = 6; measured n = 3).

$$\sigma_c/|\sigma_t| = 0.81m_i + 7 \quad (1)$$

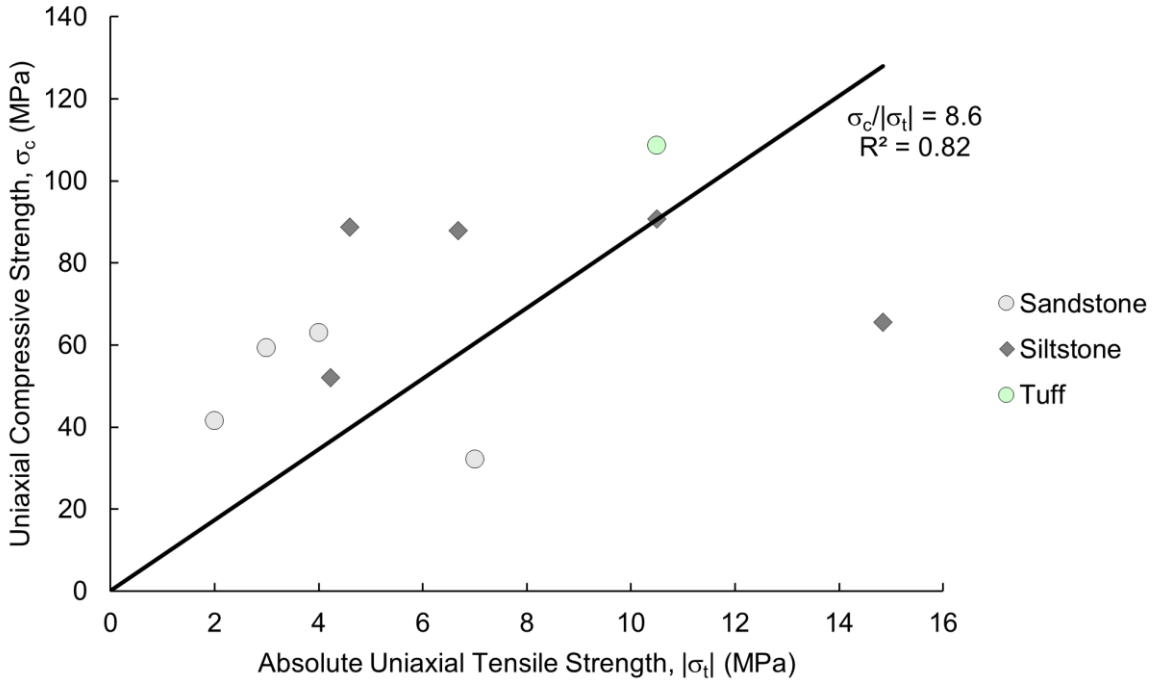

Figure 9: Relationship between σ_c and $|\sigma_t|$ by rock type for the E seam floor

Table 3: Summary of measured and empirical Hoek-Brown constants for the E seam floor

Depth below E Seam Floor (m)	Logged Lithology	Data Type*	Compressive-Tensile Strength Ratio, $\sigma_c/|\sigma_t|$	Hoek Brown y-intercept constant, σ_{ci} (MPa)	Hoek-Brown shape constant, m_i
5.30	Tuff	Measured		22.4	8.7
13.78	Siltstone	Empirical	19.3		15.2
16.17	Sandstone	Empirical	18.6		14.3
19.43	Sandstone	Empirical	13.0		7.4
22.16	Siltstone	Empirical	13.2		7.6
25.62	Siltstone	Empirical	12.3		6.5
35.10	Sandstone	Measured		35.5	9.6
39.01	Sandstone	Empirical	12.6		6.9
39.20	Sandstone	Measured		58.0	17.4

*Empirical values estimated from relationship with $\sigma_c/|\sigma_t|$ proposed by Hoek and Brown (2019).

A secant modulus ratio of 304 was found from a cross-plot of the secant Young's moduli, $E_{i,secant}$, and peak compressive stresses, σ_c, measured from UCS tests (**Figure 10**). Average secant Poisson's ratios, $\nu_{i,secant}$, of 0.24, 0.20, and 0.11 were found for sandstones, siltstones, and tuffs respectively. No relationship between Poisson's ratio and any other variable was identified.

DSS test results were overall inconclusive as they were biased towards stronger samples without significant surficial infilling and returned typical planar-rough Mohr-Coulomb friction angles of around 30°. The lack of representative DSS tests for the weak surfaces that were observed in the drill core was borne in mind during the rock mass characterisation process and engineering judgment was applied.

A summary of representative laboratory properties by rock type is provided in **Table 4**. Where the sample size was sufficient (n >20), median values were used to control for the influence of outliers which tend to skew σ_c and $E_{i,secant}$ toward the upper bound, else mean values were used. For rock types with no data, general Dawson overburden values were adopted. Due to the influence of small-scale fractures (cleat), laboratory-scale coal is much closer to the representative elementary volume (REV) than other rock types and laboratory-measured values are not directly representative of intact properties. Instead, generic intact coal properties were adopted from Medhurst and Brown (1998).

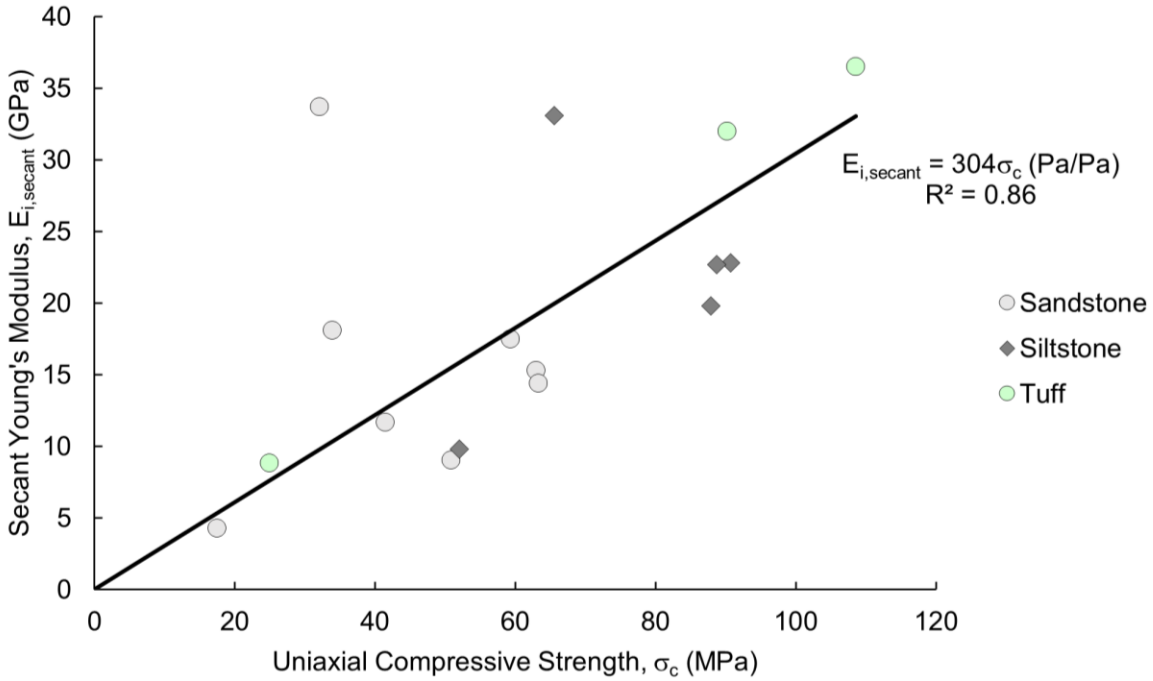

Figure 10: Cross-plot of the secant Young's modulus and UCS for the E seam floor showing a general secant modulus ratio of 304

Table 4: Summary of representative laboratory properties by rock type inferred from targeted testing of the E seam floor

Rock Type	σ_c (MPa)	$\lvert\sigma_t\rvert$ (MPa)	$E_{i,secant}$ (GPa)*	$\nu_{i,secant}$	m_i	Comment
Sandstone	45.2	3.2	13.7	0.24	11.1	Direct outputs from targeted E seam floor testing program.
Siltstone	76.7	5.0	23.4	0.21	9.8	
Tuff	74.6	7.8	22.7	0.11	8.7	
Mudstone	42.0	5.3	12.8	0.26	8.0	No data – adopted general Dawson overburden properties.
Claystone	21.0	2.6	6.4	0.26	8.0	
Carb. Siltstone	24.0	3.0	7.3	0.21	8.0	
Carb. Mudstone	21.0	2.6	6.4	0.26	8.0	
Conglomerate	108.0	4.2	32.8	0.15	26.0	
Coal	32.7	4.1	9.9	0.30	15.6	Properties for dull coal representative of intact coal (after Medhurst and Brown, 1998).

*Calculated from representative σ_c and generic secant modulus ratio of 304 Pa/Pa.

Rock Mass Downgrading

The mechanical properties of rock mass units (RMUs) below the tuffaceous claystone unit at 11.2 m depth were derived using an internal AAMC downgrading method (**Figure 11**) based on the Generalised Hoek-Brown failure criterion (Hoek et al., 2002) and the quantified Geological Strength Index (GSI) classification system (Hoek et al., 2013). Application of the Hoek-Brown-GSI system is predicated on the assumption of isotropic and homogeneous rock mass conditions and therefore has some inherent limitations for anisotropic and heterogeneous coal measure rock masses. It is also independent of scale

and requires the practitioner to ensure that appropriate consideration is given to the REV of the particular rock mass and whether any transitional materials are present (Carvalho et al., 2007; Carter et al., 2008). However, it is the only system that provides a practicable link to mechanical properties for use in numerical models. To overcome the intrinsic limitations of the basic Hoek-Brown-GSI system, the AAMC downgrading method includes additional engineering judgment-based downgrading factors for intact rock scale, anisotropy, and moisture sensitivity effects.

The characterised E seam floor RMUs and their associated mechanical properties are summarised in **Table 5**. As approximately the first 11-12 m of the spoil drillhole below the E seam floor intercepted the zone of influence of a previous floor disruption blast, generic Bowen Basin Mohr-Coulomb properties after Simmons (2020) were adopted in numerical models down to the roof of the tuffaceous claystone at 11.2 m depth. Despite this limitation, numerical models based on the characterised RMUs were able to accurately reproduce displacements measured in the field by radar monitoring, enabling:

- Prediction of displacement rates for the higher risk section of strip E16 within the extents of the tension cracks observed in strip E15.
- The use of an adaptive buttress retreat mining method with slope performance in earlier stages dictating maximum slot widths in later stages.

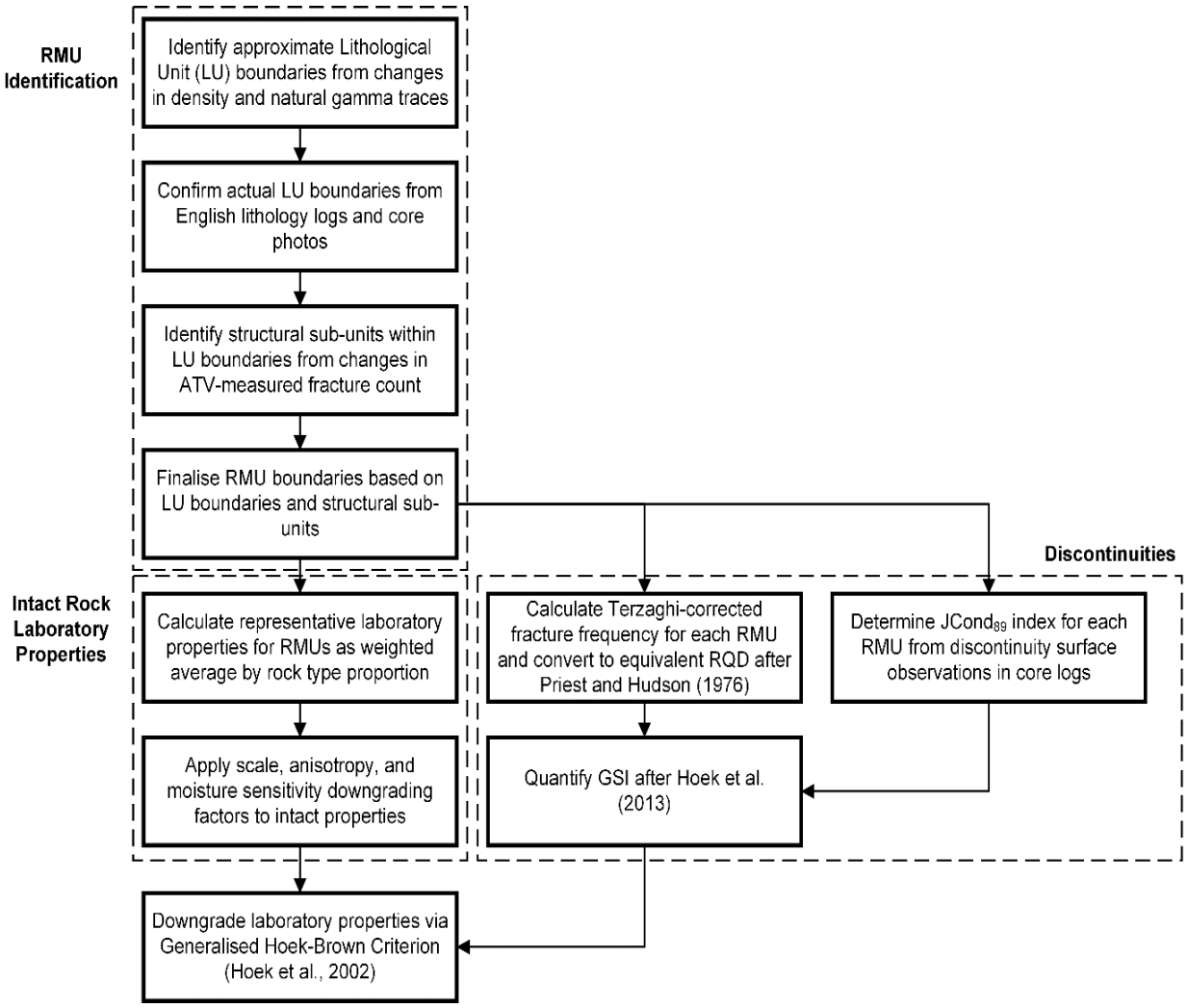

Figure 11: AAMC rock mass downgrading process based on the Generalised Hoek-Brown failure criterion and the quantified GSI

Table 5: Summary of characterised RMUs with downgraded mechanical properties

RMU #	Lithologies	Depth below E Floor From (m)	Depth below E Floor To (m)	Constitutive Model	Generalised Hoek-Brown Properties											Mohr-Coulomb Properties	
					GSI	D	σ_{ci} (MPa)^	σ_c (MPa)	σ_{cm} (MPa)	m_b	s	a	$\lvert\sigma_{tm}\rvert$ (kPa)	E_m (GPa)#	ν_m&	c (kPa)	ϕ (°)
1	Generic fresh non-coal*	0	11.20	Mohr-Coulomb	N/A								45	2.5	0.25	450	42
2	Tuffaceous Claystone	11.20	11.53		N/A								0	0.10	0.28	0	12
3	Siltstone (49%) Mudstone (40%) Sandstone (10%) Tuff (1%)	11.53	14.89	Hoek-Brown	70	0	47.98	9.02	14.58	4.19	0.0357	0.5014	204	10.44	0.22	N/A	
4	Tuff (62%) Sandstone (30%) Siltstone (8%)	14.89	18.37		70	0	52.77	9.92	15.59	3.90	0.0357	0.5014	241	10.43	0.22	N/A	
5	Mudstone (40%) Carb. Siltstone (26%) Coal (13%) Siltstone (12%) Tuff (7%) Core Loss (2%)	18.37	20.64		45	0	35.21	1.40	5.08	1.40	0.0022	0.5274	28	2.40	0.25	N/A	
6	Siltstone (58%) Sandstone (23%) Mudstone (16%) Coal (1%) Tuff (1%) Carb. Siltstone (1%)	20.64	33.06		70	0	50.70	9.48	16.07	4.70	0.0357	0.5029	192	10.24	0.22	N/A	
7	Coal (62%) Tuff (12%) Siltstone (9%) Carb. Siltstone (7%) Sandstone (3%) Carb. Mudstone (3%) Mudstone (1%) Claystone (1%) Core Loss (1%)	33.06	37.06		49	0	38.43	1.30	5.44	2.25	0.0035	0.5978	30	3.23	0.25	N/A	
8	Sandstone (96%) Conglomerate (3%) Siltstone (1%)	37.06	50.00		70	0	37.91	7.13	12.30	4.92	0.0357	0.5014	137	7.52	0.22	N/A	

*After Simmons (2020).
^The intact Hoek-Brown constant, σ_{ci}, is reported alongside the downgraded rock mass mechanical properties as it is required as an input to FLAC3D.
#Rock mass Young's modulus downgraded according to Hoek and Diederichs (2006).
&Rock mass Poisson's ratio adjusted according to formula (Clark, pers. comm.): $\nu_m = 0.32\text{-}0.0015GSI$.

NUMERICAL MODELS

Approach

A series of numerical models were undertaken to:

- Predict likely displacement magnitudes and extents with respect to the as-designed strip E16 slope geometry; and
- Recommend slot widths for a buttress retreat mining sequence to find an optimal balance between safety and economics.

Conventional limit equilibrium methods that are commonly used in the Australian coal mining industry for lowwall design were not suitable as they do not consider deformability properties and are restricted to 2D. Instead, Itasca Consulting Group's FLAC3D continuum numerical modelling code was identified as a more appropriate tool. AAMC has recently acquired internal FLAC3D capabilities and the models were therefore developed in-house. An advantage of in-house development is the ability to re-run models as new data are acquired without incurring additional consulting fees. This enabled an incremental approach to modelling wherein they were incrementally improved throughout the mining process.

Preliminary Mechanistic Models

In accordance with the modelling philosophy advocated by Starfield and Cundall (1988) and illustrated in **Figure 12**, the models were initially developed primarily as mechanistic models to firstly identify the likely extents of relative displacement magnitudes. Spoil was treated as a category 2.5 material within the generic spoil framework proposed by Simmons and McManus (2004). A generic Young's modulus of 30 MPa and Poisson's ratio of 0.3 were used for all spoil. The development of displacements with respect to the base case with fixed 100 m slot widths are shown in **Figure 13**. Practically, these results were interpreted to mean that:

- The slope was inherently unstable and likely to express large-scale displacements irrespective of the chosen slot width.
- Despite common treatment of lowwall stability as an idealised 2D problem, in this case the instability was one large, interconnected 3D system controlled by the weak floor horizon, with excavation in the southern end of the pit affecting the northern half of the slope more than 1 km away.
- A risk-dependent variable slot width, where risk is proportional to the location and extents of elevated displacement magnitudes, could be used to:
  a) Control local bench-scale instabilities; and
  b) Arrest the rate of displacement.

Typical situation	Complicated geology; inaccessible; no testing budget	⟷	Simple geology; $$$ spent on site investigation
Data	None	⟷	Complete
Approach	Investigation of mechanisms	⟷ Bracket field behaviour by parametric studies ⟶	Predictive (direct use in design)

Figure 12: Spectrum of modelling scenarios showing the recommended modelling approach with respect to the quality of data inputs. Modified from Itasca Consulting Group (2020)

Adaptive Mining Sequence

A sensitivity analysis of fixed buttress slot widths of 50 m and 200 m led to the development of the initial mining sequence shown in **Figure 14**. Given the relatively low initial confidence in the model results, an adaptive approach based on the Observational Method (Terzaghi, 1943; Peck, 1969; Fairhurst, 2017) was recommended wherein observations in earlier slots could be used to adjust later slot widths. A

400 m wide initial slot was therefore recommended from CH0 to CH400 where displacements were anticipated to be at a minimum. The slot width then reduced to a nominal 200 m as the retreat approached the critical CH1000 transition point. Directly within the elevated risk area from CH1000 to CH1900, slot widths reduced to a nominal 100 m.

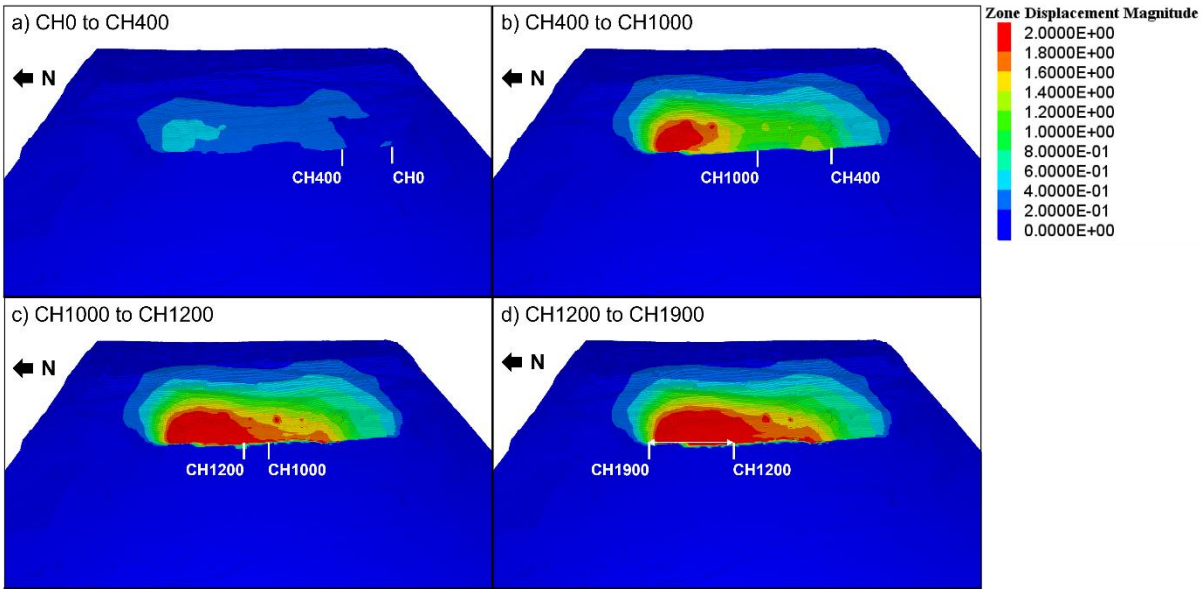

Figure 13: Evolution of displacements in the strip E16 preliminary mechanistic model

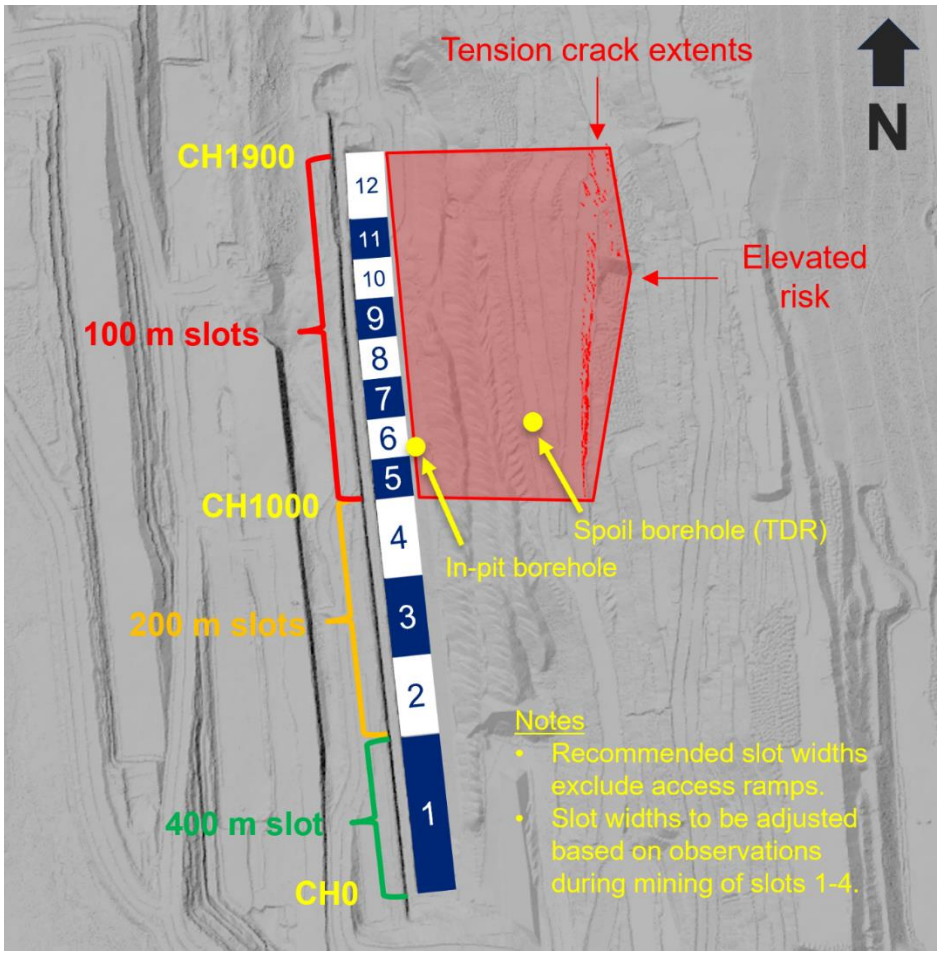

Figure 14: Initial mining sequence recommended based on preliminary mechanistic models

During de-coaling of slot 1 from CH0 to CH400, increases in the dimensionless TDR reflection coefficient, which can be assumed proportional to displacement, were observed at a depth of 11-12 m below the E seam floor, coinciding with the tuffaceous claystone unit (**Figure 15**). While this would normally be surprising given that the TDR was installed at CH1200, the observation was consistent with the numerical model and highlights that lowwall active-passive wedge mechanisms are in fact 3D problems despite their common treatment as idealised 2D sections. However, unlike the numerical models, the subsurface displacements did not initially manifest as surficial displacements that could be detected by radar monitoring. This was taken to indicate that the numerical model deformability inputs were conservative, which was acceptable given that it was at this stage a preliminary mechanistic model rather than a necessarily predictive one. An alternative hypothesis was that the TDR had intersected the updip active wedge but the resultant driving force was not yet sufficient to mobilise the downdip passive wedge at displacement rates detectable by radar, but this could not be conclusively proven.

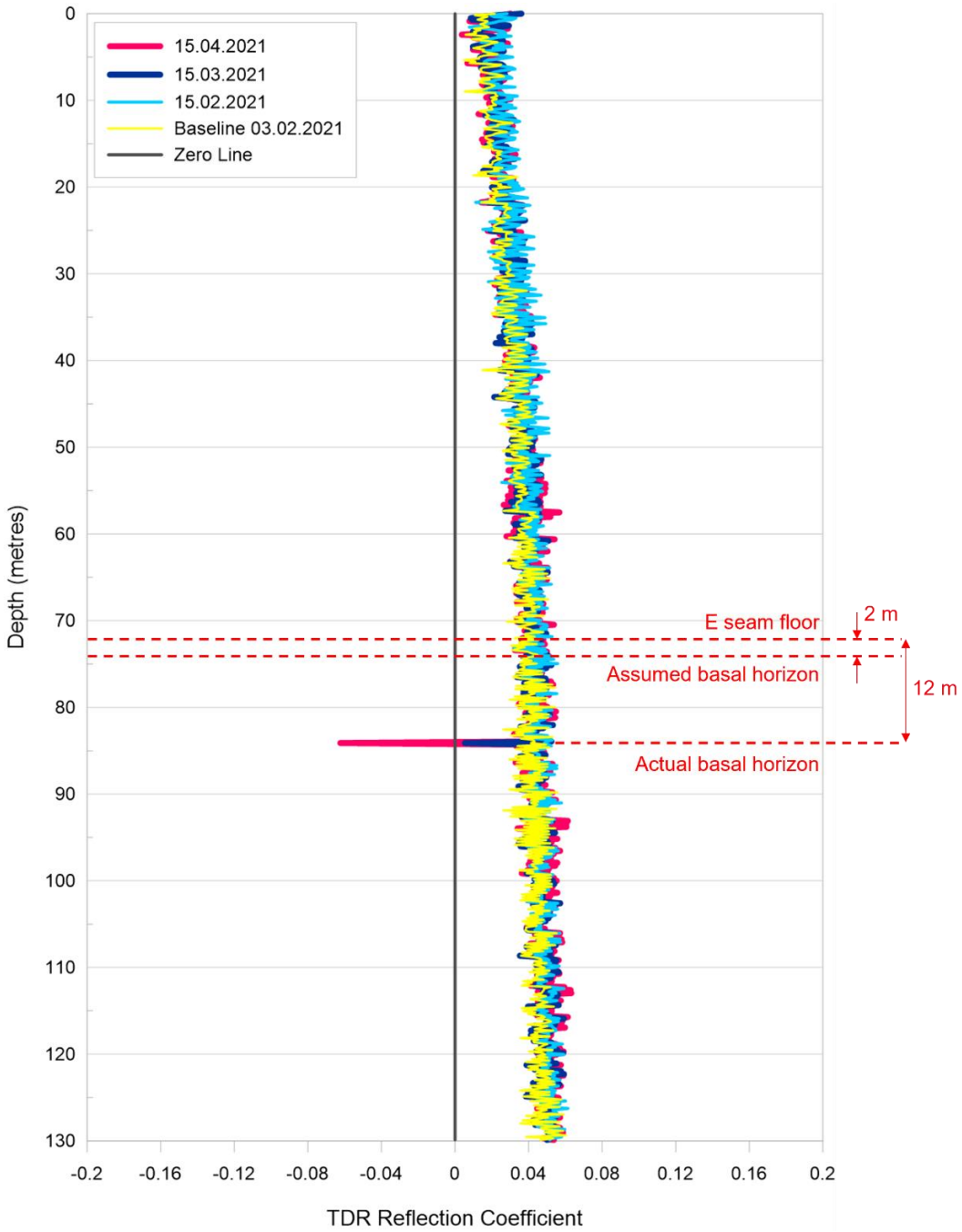

Figure 15: Sub-surface shear displacements measured by a TDR installed in the Pit 6-8 E16 lowwall at CH1200 showing a basal instability horizon 11-12 m below the E seam floor

As mining progressed further north, the rate of absolute change in the TDR reflection coefficient, |ΔTDR|, continued to increase until the TDR cable was rendered inoperable shortly after de-coaling from CH400 to CH1000 (**Figure 16**). However, it had served its purpose as it identified the 12 m horizon as the sole basal unit controlling the instability. As radar-measured displacement rates were overall regressive (Broadbent and Zavodni, 1982) and the extents were broadly consistent with those predicted by the numerical models, confidence was gained in the slope performance and the likelihood of a sudden collapse was considered low. The actual slot widths beyond CH1000 were therefore increased to 200 m from the 100 m in the initial mining sequence in **Figure 14**. Displacement modes remained regressive and strip E16 was completed safely without coal sterilisation.

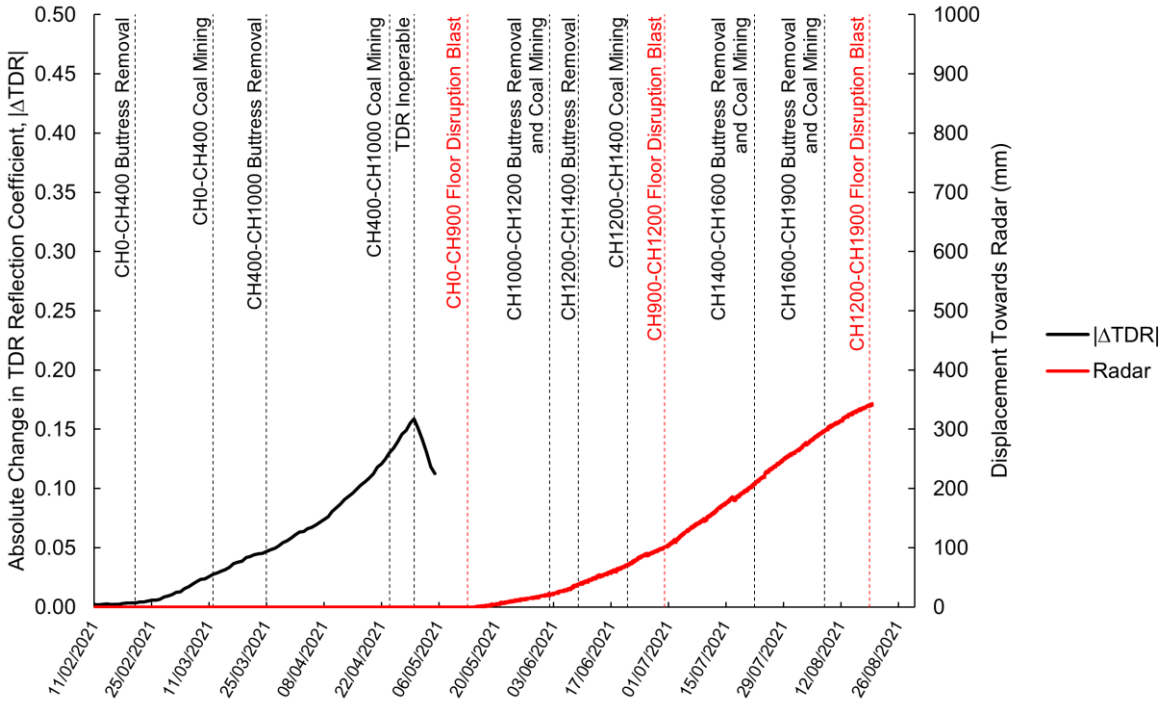

Figure 16: TDR and radar displacements at CH1200

Reconciliation

Following completion of mining and monitoring in strip E16, a reconciliation process was undertaken to close the design loop and provide a validated model for use as a predictive tool in future strips. In particular, the spoil Young's modulus was modified until the modelled displacement magnitudes and extents were consistent with TDR and radar measurements, with final moduli of 100 MPa for the more consolidated old spoil prior to strip E16 and 40 MPa for the freshly emplaced spoil in strip E16. Cross-sections of pertinent model outputs at the critical CH1200 are presented in **Figure 17** and demonstrate the consistency between the model results and the field observations, including:

- Extents of displacement magnitude contours consistent with the extents of tension cracks observed in the field.
- Vertical velocity contours showing the downward movement of the updip active wedge driving the overall mechanism with back- and mid-scarps of 63° and 52° respectively.
- Maximum shear strain increment contours showing mobilisation of the instability along the weak basal horizon 11-12 m below the E seam floor.
- Local factor of safety (FOS) contours showing the variation of the internal stability state throughout the slope. Note that the local FOS for each zone was taken as the minimum of the local tensile and compressive FOS.

A comparison of the reconciled displacement-time curves measured by radar and predicted by the numerical model is provided in **Figure 18**. As the numerical timestep in FLAC3D is not automatically calibrated to real time, the time scale of the numerical displacement-time curve had to be adjusted to

match the radar curve, resulting in a conversion factor of 0.32 hours/step. As per the modelling approach previously outlined in **Figure 12**, the set of numerical model data inputs is now considered close enough to "complete" to justify the use of the model as a predictive tool to inform Trigger Action Response Plan (TARP) thresholds in future strips.

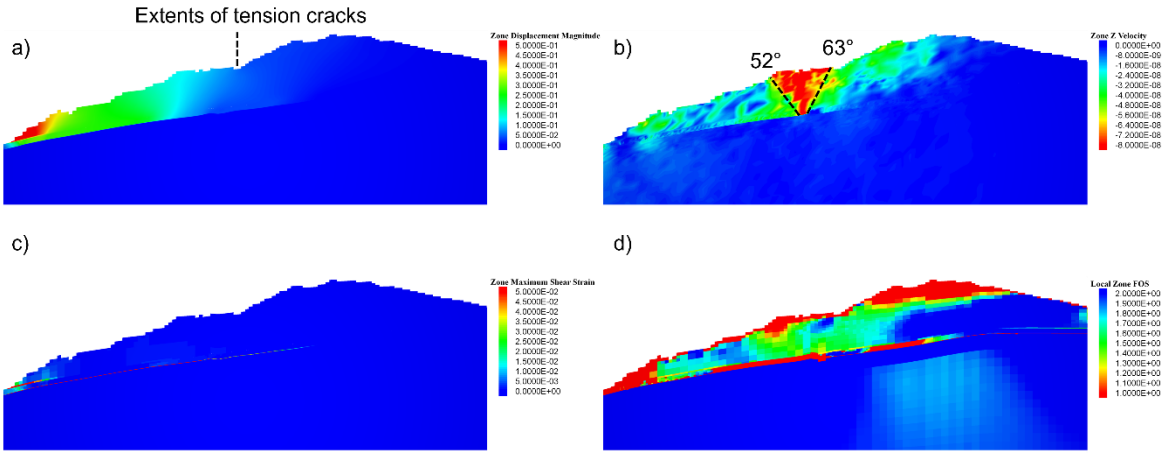

Figure 17: Cross-section of FLAC3D models at CH1200: a) displacement magnitude contours; b) vertical velocity contours; c) maximum shear strain increment contours; and d) local zone FOS contours

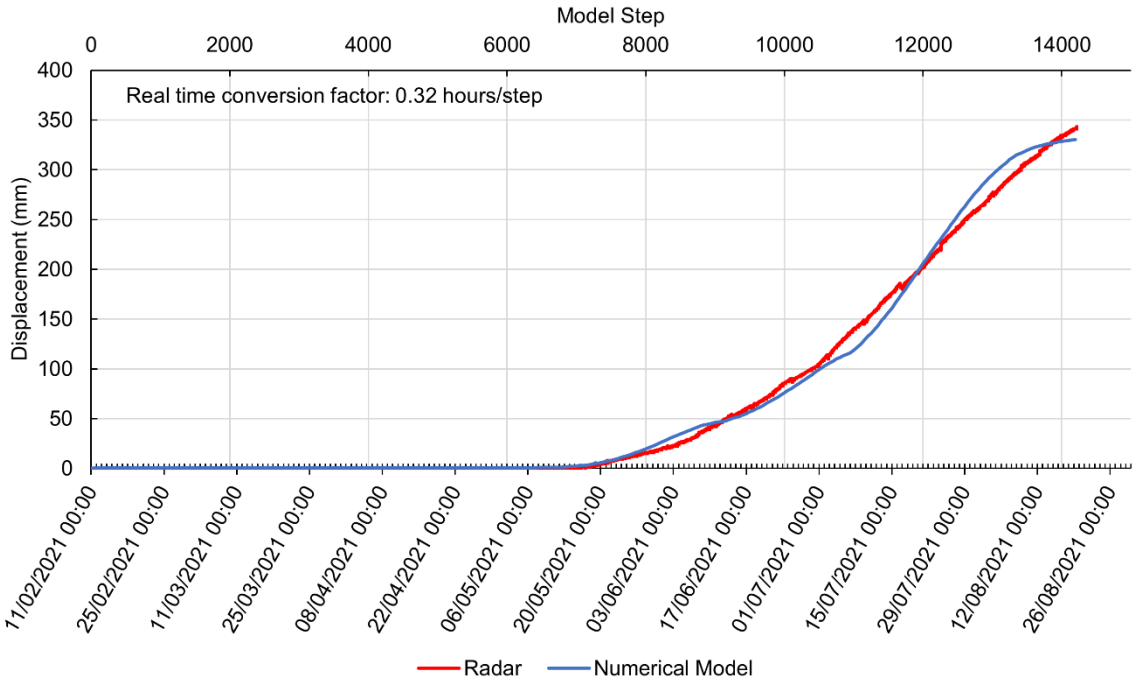

Figure 18: Reconciled displacement-time curves predicted by the numerical model and measured by radar for strip E16

DISCUSSION

Sampling and testing horizons

Prior to the Pit 6-8 lowwall instability, AAMC standards required drilling to a depth of only 3 m below the target seam floor, which is a common depth for active-passive wedge lowwall instability mechanisms in the Bowen Basin. Evidently, this depth was insufficient for the Pit 6-8 case in which the basal horizon controlling the instability was proven by subsurface TDR monitoring to be 11-12 m below the E seam floor, coinciding with a moisture-sensitive tuffaceous claystone comprised of a high proportion of mixed

layer illite-smectite swelling clays. The key factor in the Pit 6-8 lowwall instability was therefore an unknown critically weak basal horizon at the design stage. The standard drilling depth has since been updated to a minimum of 20 m below the target seam floor for all geotechnical boreholes.

Proactive identification of problematic clays

Non-routine soil mechanics tests were critical to inferring the mechanical properties of the weak tuffaceous claystone that acted as the basal horizon for the Pit 6-8 lowwall instability. In this instance, drilling was conducted post-mining when there had been a high degree of remoulding and water exposure and the problematic unit was therefore obvious. However, this will not always be the case as moisture-sensitive units may not be apparent if not yet exposed to water. New technologies that would enable the rapid, cost-effective, and proactive identification of problematic clay minerals before the design stage would therefore be most welcome. The technologies would ideally provide a continuous log of mineralogical composition by depth as opposed to the discrete nature of XRD and SD testing which require targeted point sampling by a human. Previous ACARP-funded research (Fraser et al., 2006) applied a hyperspectral core scanning technique to Bowen Basin and Hunter Valley coal and overburden materials but the researchers noted challenges in separating mixed-layer illite-smectites from other clay types. Sullivan (2011) compared the hyperspectral technique with conventional XRD analysis for the Alpha Coal Project in the Galilee Basin and reached similar conclusions to Fraser, but also suggested that XRD analysis may underestimate the mixed-layer illite-smectite content with some proportion being unidentified in the residual “amorphous” category. More recent ACARP-funded research (Manlapig et al., 2018) combined hyperspectral imaging technology with computed tomographic scanning for coal quality analysis and recommended future upscaling to a high-resolution wireline technique. Clearly, there has been industry appetite for such technologies in the past and future investment is encouraged given the significant risk of surprise instabilities associated with unknown clay mineralogy.

Groundwater

The VWP measurements from the spoil borehole are shown in **Figure 19** with respect to key stages in the strip E16 mining sequence. A gradual reduction in groundwater head of around 5 m during excavation from CH0 to CH1000 is observed and is inferred to be related to stress relief resulting from mining activity. VWPs 1 to 3, which were installed between 33.5 m and 53.5 m below the E seam floor, were all rendered inoperable over a 1-week period following the CH0 to CH900 floor disruption blast. This was not interpreted to be related to the blast, rather the timing was likely coincidental as a result of excessive accumulated displacements shearing the VWP cables off at the tuffaceous claystone horizon. VWP4 never recorded any data and was assumed to be inoperable from installation. VWP5, which was the only VWP installed above the basal horizon controlling the instability, showed large fluctuations in groundwater heads throughout the mining sequence. The initial reduction in groundwater head from February to April was attributed to grout curing and therefore considered erroneous. From April to August in which buttress removal and coal mining were focused closer to the spoil borehole, large increases in groundwater head up to 30 m were recorded by VWP5. There were no major rainfall events in this period that could explain the increase. Following discussion with the supplier, it was hypothesised that the creation of a grout bulb around the VWP5 sensor during installation may have caused the possibly anomalous result, but at the time of writing the precise cause remains unverified. A hydrogeology expert has been engaged by AAMC to interpret the results but for the purpose of the numerical models, groundwater was represented as a typical phreatic surface 5 m above the E seam floor drawing down to the lowwall toe. This may be revisited in future models pending outcomes of the hydrogeological assessment.

Floor treatment options

It was hypothesised that the zone of influence associated with the historical 10 m floor disruption blast depth was potentially coinciding with the roof of the tuffaceous claystone unit at 11-12 m depth and inducing dilation, weakening it further in addition to any degradational effects resulting from displacement-related remoulding. It was then proposed that future floor treatment blasts could be extended at least a few metres into the stronger rock mass unit immediately below the tuffaceous claystone. However, during drilling of deeper floor treatment blastholes in the northern half of strip E16, systemic closure was observed in all blastholes at a depth consistent with the tuffaceous claystone (**Figure 20**). At the time of writing, there is on-going investigation to assess floor treatment options and alternative measures for arresting displacement rates should it not be possible to extend blasting depths. As demonstrated by recent ACARP-funded research (Onederra et al., 2021), floor disruption blasting is

a complex problem requiring consideration of many factors that are challenging to represent in numerical models, particularly for deeper horizons at which confining stresses are higher and the effectiveness of disruption blasting is reduced. Specifically, the dynamic strain rates associated with the sudden impact of a blast require consideration of variable tensile strengths and damping coefficients. This is an area in need of further research.

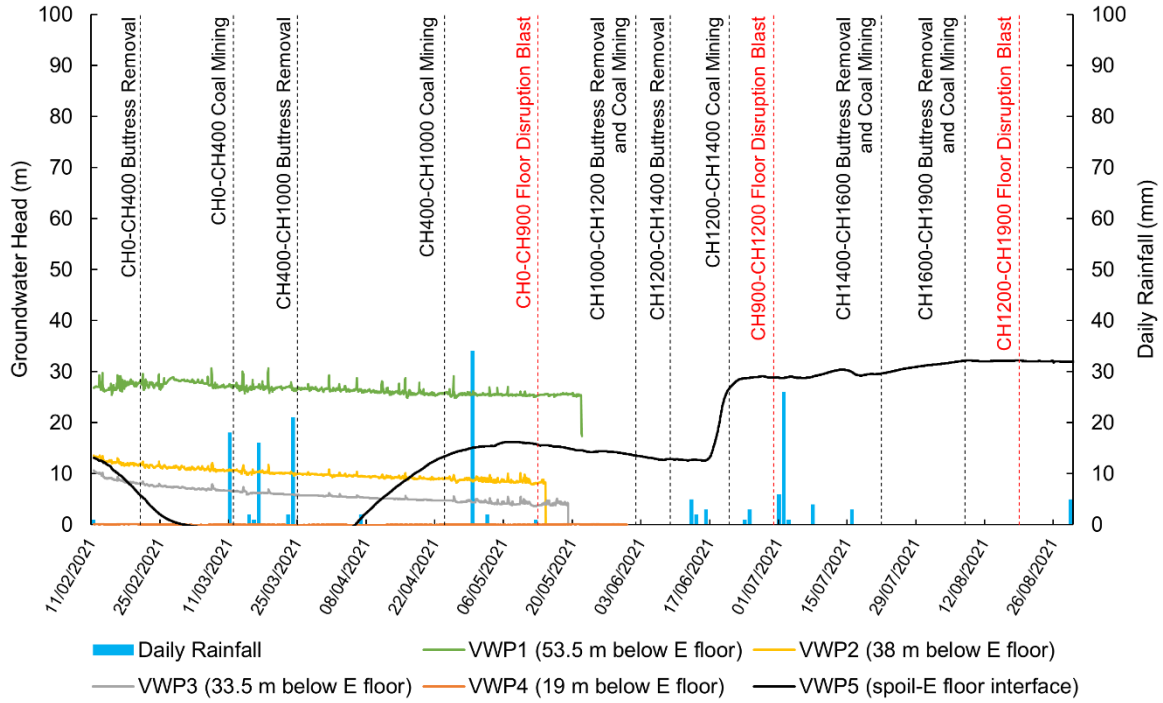

Figure 19: Vibrating Wire Piezometer measurements in spoil borehole at CH1200

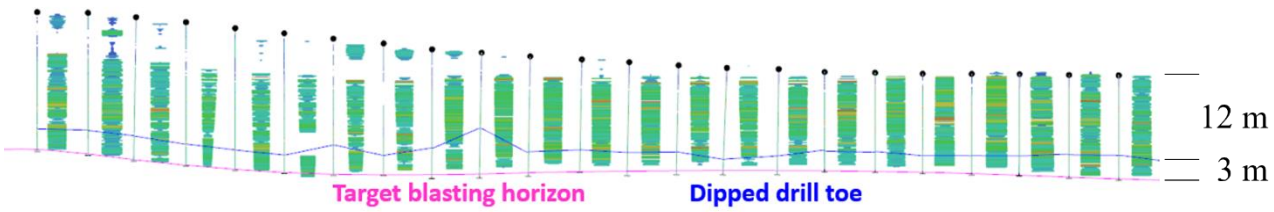

Figure 20: Systemic blockages of strip E16 floor treatment blastholes during attempted dipping

CONCLUSIONS AND RECOMMENDATIONS

The Dawson Pit 6-8 lowwall instability was a deep-seated active-passive wedge mechanism that mobilised in strip E15 along a previously unknown weak unit 11-12 m below the lowwall floor. XRD analysis revealed that the weak unit, which had previously been logged as a tuffaceous sandstone, was in fact a tuffaceous claystone comprised of a significant proportion of mixed-layer illite-smectite swelling clays. Slake durability analysis returned first and second cycle durability indices of 2.2% and 0.1% respectively, consistent with an extremely moisture-sensitive material. A novel soil mechanics approach was then applied to derive shear strength properties for the tuffaceous claystone while an internal AAMC rock mass characterisation process based on the Hoek-Brown-GSI system was used to characterise the remainder of the more competent E seam floor rock mass. The characterised mechanical properties were then used in large-scale 3D numerical models to optimise the buttress retreat slot width for strip E16. During mining of strip E16, a TDR installed within the footprint of the unstable lowwall confirmed basal mobilisation of the instability along the tuffaceous claystone. Although the pit economics were affected by the switch from a conventional forward pass to a retreat buttress method with backfilling of each slot after de-coaling, strip E16 was completed safely without coal sterilisation.

As the numerical models were developed in-house, AAMC now has a validated 3D numerical model of the Pit 6-8 lowwall instability that can be re-used in future for rapid and cost-effective predictive stability modelling to inform the planning of strips E17+. However, there is on-going work to better understand the impacts of groundwater and blasting modifications to ensure that high quality model inputs are available. Further, general improvement in the proactive identification of problematic clay minerals is needed as XRD analysis is not currently routine and produces only discrete point data based on human interpretation at the core sampling stage. Hyperspectral core scanning technologies appear promising in this regard and would ideally be developed into another wireline tool that can produce a continuous downhole plot of mineralogical composition for comparison with the standard suite of geophysical tools at the slope design stage.

ACKNOWLEDGEMENTS

The authors wish to acknowledge the contributions of: Dr. Ian Clark (GEONET Consulting Group) for advising and reviewing the numerical models; Mr. Paul Maconochie for discussions around mechanical downgrading of clay-rich rock types; Em. Prof. Joan Esterle for discussions around the nature of the Kaloola Member and hyperspectral technologies; and Dr. John Simmons (Sherwood Geotechnical and Research Services) for identifying the previously unconsidered Kaloola Member as a potential basal control for the instability mechanism and providing input to the subsequent exploration program. Finally, Dawson Mine management is thanked for allowing us to disseminate the information.

REFERENCES

Brace, W F, Paulding, J B W and Scholz, C, 1966. Dilatancy in the fracture of crystalline rocks, *Journal of Geophysical Research,* 71:3939-3954.

Broadbent, C D and Zavodni, Z M, 1982. Influence of rock structure on stability, in *Stability in Surface Mining, Vol. 3* (Society of Mining Engineers).

Carter, T G, Diederichs, M S and Carvalho, J L, 2008. Application of modified Hoek-Brown transition relationships for assessing strength and post yield behaviour at both ends of the rock competence scale, *Journal of The Southern African Institute of Mining and Metallurgy*, 108:325-338.

Carvalho, J L, Carter, T G and Diederichs, M S, 2007. An approach for prediction of strength and post yield behaviour for rock masses of low intact strength, in *Proceedings 1st Canada-US Rock Symposium: Meeting Society's Challenges and Demands*, pp 249-257 (American Rock Mechanics Association).

Fairhurst, C, 2017. The observational approach in rock engineering, *Hydraulic Fracturing Journal*, 4:36-41.

Fraser, S, Esterle, J, Ward, C, Henwood, R, Mason, P, Huntington, J, Connor, P, Sliwa, R, Coward, D and Whitbourn, L, 2006. Automated mineralogical logging of coal and coal measure core, ACARP project C13014, CSIRO Energy Technology, University of NSW.

Gonano, L P, 1980. An Integrated Report on Slope Failure Mechanisms at Goonyella, Technical Report Number 114, CSIRO Division of Applied Mechanics.

Hoek, E and Brown, E T, 1997. Practical estimates of rock mass strength, *International Journal of Rock Mechanics and Mining Sciences,* 34:1165-1186.

Hoek, E and Brown, E T, 2019. The Hoek-Brown failure criterion and GSI – 2018 edition, *Journal of Rock Mechanics and Geotechnical Engineering*, 11:445-463.

Hoek, E, Carranza-Torres, C and Corkum, B C, 2002. Hoek-Brown failure criterion – 2002 edition, *paper presented at 5th North American Rock Mechanics Symposium and the 17th Tunnelling Association of Canada Conference: NARMS-TAC* (Tunnelling Association of Canada: Toronto).

Hoek, E and Diederichs, M S, 2006. Empirical estimation of rock mass modulus, *International Journal of Rock Mechanics and Mining Sciences*, 43:203-215.

Hoek, E, Carter, T G, and Diederichs, M S, 2013. Quantification of the Geological Strength Index chart, *paper presented at the 47th US Rock Mechanics / Geomechanics Symposium*, San Francisco, USA, 23-26 June.

Itasca Consulting Group, 2020. FLAC3D version 7.0 [online]. Available from: https://www.itascacg.com/software/flac3d [Accessed: 16 November 2020].

Leisemann, B E, Follington, I L, Lohe, E M, McLennan, T P T, Fielding, C and Miller, D, 1992. Highwall mining project Moura Mine, Review of the geological and geotechnical environment of Moura Mine, QLD, CSIRO Division of Geomechanics, Australia.

Manlapig, E, Shi, F, Nguyen, A K, Jackson, J, Esterle, J, Rodrigues, S, Liu, H, Pretorius, S and Fonteneau, L, 2018. Acquisition of coal quality by semi-automatic analysis of Corescan HCI-3 system (hyperspectral) and other images, ACARP project C25028, Julius Kruttschnitt Minerals Research Centre, University of Queensland, Corescan Pty Ltd.

Medhurst, T and Brown, E T, 1998. A study of the mechanical behaviour of coal for pillar design, *International Journal of Rock Mechanics and Mining Sciences,* 35:1087-1105.

Nicksiar, M and Martin, C D, 2013. Crack initiation stress in low porosity crystalline and sedimentary rocks, *Engineering Geology*, 154:64-76.

Onederra, I, Chacon, F and Kanchibotla, S, 2021. Improving blasting outcomes and reducing geotechnical risks, ACARP project C28041, University of Queensland.

Peck, R B, 1969. Ninth Rankine Lecture: Advantages and limitations of the observational method in applied soil mechanics, *Géotechnique*, 19:171-187.

Perras, M A and Diederichs, M S, 2014. A review of the tensile strength of rock: concepts and testing, *Geotechnical and Geological Engineering,* 32:525-546.

Priest, S D and Hudson, J A, 1976. Discontinuity spacings in rock, *International Journal of Rock Mechanics and Mining Sciences and Geomechanics Abstracts,* 13:135-148.

Simmons, J V and McManus, D, 2004. Shear strength framework for design of dumped spoil slopes for open pit coal mines, in *Proceedings Advances in Geotechnical Engineering: The Skempton Conference (eds. Jardin, R J, Potts, D M and Higgins, K G)*, pp 981-991 (Thomas Telford: London).

Simmons, J V, 2020. Geomechanics of Australian open cut coal mining, in *Proceedings International Symposium on Slope Stability in Open Pit Mining and Civil Engineering, Slope Stability 2020 (ed. Dight, P M)*, pp 39-64 (Australian Centre for Geomechanics: Perth).

Sliwa, R, Esterle, J, Phillip, L and Wilson, S, 2017. Rangal Supermodel 2015: the Rangal-Baralaba-Bandanna Coal Measures in the Bowen and Galilee Basins, ACARP project C22028, University of Queensland.

Sliwa, R, Hamilton, S, Hodgkinson, J and Draper, J, 2008. Bowen Basin structural geology 2007 – a new interpretation based on airborne geophysics, paper presented at PESA Eastern Australian Basins Symposium III, Sydney, 14 - 17 September.

Starfield, A M and Cundall, P A, 1988. Towards a methodology for rock mechanics modelling, *International Journal of Rock Mechanics and Mining Sciences and Geomechanics Abstracts*, 25:99-106.

Sullivan, T, 2011. Clay mineralogy, chemical and geotechnical interrelationships in Cenozoic and Permian strata, and potential impacts on proposed mining at the Alpha coal Project, Eastern Galilee Basin, Queensland, BSc thesis (unpublished), University of Queensland, Brisbane.

Terzaghi, K, 1943. *Theoretical Soil Mechanics* (John Wiley and Sons, Inc.: New York).

Terzaghi, R, 1965. Sources of error in joint surveys, *Géotechnique*, 15:287-304.